Journal of The Electrochemical Society

OPEN ACCESS

Growth Kinetics of Multi-Oxide Passive Film Formed Upon the Multi-Principal Element Alloy AlTiVCr: Effect of Transpassive Dissolution of V and Cr

To cite this article: S. Choudhary *et al* 2021 *J. Electrochem. Soc.* **168** 051506

Journal of The Electrochemical Society, 2021 **168** 051506

Growth Kinetics of Multi-Oxide Passive Film Formed Upon the Multi-Principal Element Alloy AlTiVCr: Effect of Transpassive Dissolution of V and Cr

S. Choudhary,[1,z] S. Thomas,[1] D. D. Macdonald,[2,*] and N. Birbilis[3,*]

[1]*Department of Materials Science and Engineering, Monash University, VIC 3800, Australia*
[2]*Department of Nuclear Engineering, University of California at Berkeley, Berkeley, California 94720, United States of America*
[3]*College of Engineering and Computer Science, Australian National University, ACT 2601, Australia*

The growth kinetics of the surface film formed upon the multi-principal element alloy AlTiVCr under anodic polarisation in 0.6 M NaCl was investigated using atomic emission spectroelectrochemistry (AESEC). The AESEC charge balance analysis revealed that thickness of the barrier layer of the passive film upon the alloy: (1) increases linearly with the increase in anodic potential during potentiodynamic polarisation, and (2) increases logarithmically with exposure time during potentiostatic polarisation. This is consistent with the assumptions of the point defect model, despite the film being a multi-oxide film with transpassive dissolution of V and Cr. The X-ray photoelectron spectroscopy (XPS) analysis suggested that the growth of the film was predominantly due to TiO_2 during anodic polarisation. The electric field was found to decrease with enrichment of TiO_2 in the barrier layer. The Mott-Schottky analysis revealed that the diffusivity of oxygen vacancies increased with the increase in fraction of TiO_2 in the film, which subsequently led to the increase in the growth rate of the barrier layer during transpassive dissolution. The present work is a discrete effort towards understanding the growth behaviour of the passive film experiencing complex and competing interfacial electrochemical processes, upon a multi-principal element alloy.

 [DOI: 10.1149/1945-7111/ac0018]

Manuscript submitted January 31, 2021; revised manuscript received April 19, 2021. Published May 19, 2021. *This paper is part of the JES Focus Issue on Characterization of Corrosion Processes in Honor of Philippe Marcus.*

Recent advances in alloy design are being applied to a broad new class of alloys, known as multi-principal element alloys (MPEA).[1] MPEAs comprise 3 to 6 alloying elements—with at least 2 alloying elements present in "principal" fractions.[2] Based on their composition and the microstructures obtained, MPEAs are also often termed high entropy alloys (HEAs) or complex concentrated alloys (CCAs).[3] In contrast to conventional single-principal element alloys (SPEA), several MPEAs have been reported to possess unique characteristics such as high strength, high fracture resistance, and high wear resistance.[4] In addition to the unique mechanical properties, many MPEAs exhibit excellent resistance to corrosion and pitting in aqueous media.[5,6] In the case of passivity of MPEAs, different factors are credited to the passivity observed for MPEAs of different compositions.[2,6]

Characteristics of the passive film that govern the corrosion behavior of an alloy include the composition, thickness, and electronic properties.[7] There is extensive literature available on the effect of such film characteristics on the corrosion performance of pure metals and SPEAs. However, detailed studies that include all these film characteristics regarding MPEAs are scarce.

X-ray photoelectron spectroscopy (XPS) analysis, being the most common approach, has been employed to characterise the passive films upon several corrosion-resistant MPEAs.[8–17] The XPS studies suggest that the passive films upon most MEPAs studied to date comprise multiple oxides in fractions that correspond to incongruent oxidation of the alloy. The passive film upon CoCrFeNi alloy was found to be enriched with Cr_2O_3, which is posited to result in the excellent corrosion resistance of the alloy.[18,19] The evolution of passive film of the CoCrFeNi system has also been studied with the addition of additional elements including Al, Mn, Mo, Ti.[9–11,19] The fraction of "protective" Cr_2O_3 in the film decreases due to the addition of such elements,[10,19] which may be attributed to a decrease in Cr content in the alloy. The barrier properties of the Cr_2O_3 rich film upon the CoCrFeNi alloy are found to decrease due to the addition of Al and Mn.[10,11] On the other hand, the addition of Ti, Mo increased the pitting potential of the CoCrFeNi systems, suggesting an increase in protectiveness of the film.[11,19] Song and Xu analysed the passive film upon $(TiZrNbTa)_{90}Mo_{10}$ alloy formed in Ringer's solution;[17] the authors reported a multi-oxide passive film enriched with TiO_2 and Ta_2O_5, responsible for the observed resistance to corrosion and pitting. In contrast, Jayaraj et al., who studied the corrosion behavior of TaNbZrHfTi alloy, did not find TiO_2, Ta_2O_5, and Nb_2O_5 protective in fluorinated nitric acid.[20]

The studies summarised above suggest that many oxides (such as Al_2O_3, Mn-oxides, and Fe-oxides) are not protective despite being thermodynamically "stable" in certain potential-pH ranges (as proposed by the Pourbaix diagram[21]). Moreover, the stability of the many protective oxides (such as Cr_2O_3, V_2O_3, MoO_2) is limited to a certain potential-pH range. The passivity in such cases depends on the synergy between different oxides present in the multi-oxide film. An atomic emission spectroelectrochemistry (AESEC) study revealed that the dissolution behavior of the AlTiVCr alloy in 0.6 M NaCl was persistent to the predicted E-pH diagram.[22] Despite transpassive dissolution of V and Cr, the AlTiVCr alloy exhibits a wide passive window during potentiodynamic polarisation in 0.6 M NaCl. Therefore, the present study aims to understand the interdependency of dissolution and growth rate of the multi-oxide film upon the AlTiVCr alloy.

In aqueous media, it is experimentally found that thickness of the passive film increases linearly with an increase in the anodic potential, whereas growth kinetics of the passive film with the exposure duration (during potentiostatic polarisation) has been described using two growth laws in literature: (1) direct-logarithmic, and (2) inverse-logarithmic. The passive films upon most valve metals (Al, Ti, Ta, Nb, Zr, Hf, Mo, etc) and conventional alloys are found to obey the direct-logarithmic growth law, irrespective of the pH of electrolytes used.[23–25] However, both direct and inverse-logarithmic growth laws have been applied in the case of Fe and Fe-Cr alloys.[26–30] Such altercations are attributed to both inverse and direct-logarithmic growth laws being mathematically equivalent when the change in the film thickness is small.[31,32] Researchers have also reported a multi-stage growth behavior of the passive film on Fe.[33–35]

Three classical models, namely the high field model (HFM),[36] place exchange model (PEM),[37] and point defect model (PDM),[38]

*Electrochemical Society Fellow.
[z]E-mail: Sanjay.Choudhary@monash.edu

proposed the direct-logarithmic growth kinetics of the passive film—with different assumptions. The HFM is one of the earliest models that initially proposed the inverse logarithmic growth law,[39] with the assumption that metal cations migrate across the film to the film-electrolyte interface due to the presence of a high electric-field ($>10^6$ V cm^{-1}), and they react with the electrolyte to result in formation and growth of the film. However, it was later found that migration of both cation and anion is responsible for the growth of the surface film.[40] Lanyon and Trapnell hypothesised that adsorbed oxygen layer on the metal surface exchanges the place between the underlying metal layer (possibly by rotation), and the surface film thickens with rotation of metal-oxygen pairs and simultaneous adsorption of a second oxygen layer.[41] Sato and Cohen adapted the "place exchange" theory and proposed logarithmic growth kinetics of the passive film during potentiostatic polarisation.[37] Fehlner and Mott modified the HFM with the adaptation of the place exchange mechanism and proposed another direct-logarithmic growth law.[36] Macdonald and co-workers[38] proposed the PDM, which postulated that the passive films upon metals and alloys contain a significant number (in the range of 10^{18}–10^{22} cm^{-3}) of ionic defects such as vacancies and interstitials; generation and annihilation of such defects at the interfaces control the growth kinetics of the films.

The PDM describes the growth of the barrier layer of a passive film using seven interfacial defect generation/annihilation reactions, shown in Fig. 1. More detail can be obtained elsewhere.[42] In short, the barrier layer is formed (at metal/barrier layer interface) and destroyed (at barrier layer/electrolyte interface) by Reactions 3 and 7 (Fig. 1), respectively. As seen in Fig. 1, Reaction 1 generates oxygen vacancies at the metal/ barrier layer interface, which are annihilated by Reaction 6 at the barrier layer/ electrolyte interface. Moreover, cation vacancies are generated at the barrier layer/ electrolyte interface and annihilated at the metal/barrier layer interface by Reactions 4 and 1, respectively. Similarly, Reactions 2 and 5 describe the generation and annihilation of metal interstitials at the metal/barrier layer interface and the barrier layer/electrolyte interface, respectively. According to the PDM, the growth rate of the barrier layer can be expressed as:[42]

$$\frac{dL}{dt} = Ae^{-bL} - C \qquad [1]$$

where $A = \Omega k_3^0 e^{\alpha_3(1-\alpha)\chi\gamma E} e^{-\alpha_3\beta\chi\gamma pH}$, $b = \alpha_3\chi\varepsilon\gamma$, $C = k_7^0 e^{\alpha_7\alpha(\delta-\chi)\gamma E} e^{\alpha_7\beta(\delta-\chi)\gamma pH}\left(\frac{C_{H^+}}{C_{H^+}^0}\right)^n$, $\gamma = F/RT$, Ω is the molar volume of the barrier layer per cation, k_i^0 is the standard rate constant of Reaction i, α is the polarizability of the barrier layer/ electrolyte interface, β is the dependence of potential drop at the barrier layer/electrolyte interface on pH, α_i is the transfer coefficient of Reaction i, ε is the electric field strength.χ and δ are the cationic charges in the film and the electrolyte, respectively. C_{H^+} is the concentration of hydrogen ion at the barrier layer/electrolyte interface, $C_{H^+}^0$ is the corresponding quantity in the standard state, and n is the kinetic order of the dissolution of the barrier layer with respect to H^+. By integrating Eq. 1, the increase in thickness of the barrier layer with increasing time during potentiostatic polarisation can be obtained as:[43]

$$L(t) = L_0 + \frac{1}{b}\ln\left[1 + \left(\frac{A}{C}\right)e^{-bL_0}(e^{bCt} - 1)\right] - Ct \qquad [2]$$

In addition, Eq. 1 yields the steady-state ($\frac{dL}{dt} = 0$) thickness of the barrier layer as:

$$L_{ss} = \frac{1}{\varepsilon}\left[1 - \alpha - \frac{\alpha\alpha_7}{\alpha_3}\left(\frac{\delta}{\chi} - 1\right)\right]E + \frac{1}{\varepsilon}\left\{\frac{2.303n}{\alpha_3\chi\gamma} - \beta\left[\frac{\alpha_7}{\alpha_3}\left(\frac{\delta}{\chi} - 1\right) + 1\right]\right\}pH + \frac{1}{\alpha_3\chi\varepsilon\gamma}\ln\left(\frac{k_3^0}{k_7^0}\right) \qquad [3]$$

The key difference in the growth hypothesis between the PDM and the other two growth models (HFM and PEM) is the nature of the electric field across the film. The PEM and HFM assumed that the electric field is dependent on the film thickness. In contrast, the PDM hypothesises that potential drop through the film changes in such a manner that the electric field remains constant with the growth of the film, and with increasing potential. In this regard, a constant electric field within the barrier layer has been demonstrated, both theoretically[44] and experimentally,[45] provided that the barrier layer is sufficiently thin (<3 nm) and is approximately so for thicknesses up to about 6 nm. To date, the PDM remains the most successful model that proposed a linear dependency of the film thickness on the applied potential (Eq. 3)—as observed for most pure metals and alloys. The PDM was also extended to explain the role of the outer precipitation layer of a passive film.[46] Although the PDM is being further modified for the passivity of alloys,[42] the contributions of microstructural features (including grain boundaries, texture, residual stresses, and second phases) on the growth kinetics of the passive film are yet to be addressed.

The PDM has been applied to explain the growth kinetics of the passive films of Cr-containing SPEAs including stainless steel[47] and

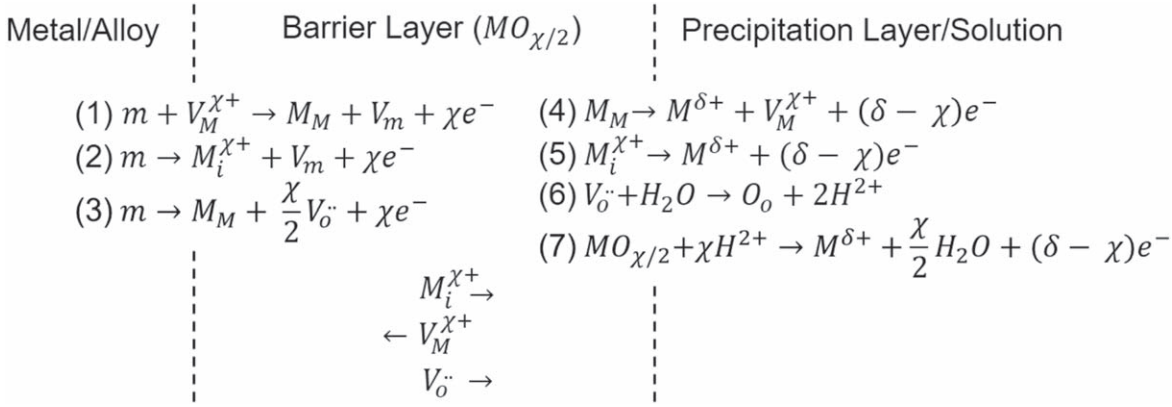

Figure 1. Interfacial defect generation/annihilation reactions responsible for the growth of passive films upon metals/alloys, as proposed by the point defect model (PDM).[42] Here m is metal atom, $V_M^{\chi'}$is cation vacancy on the metal sublattice of the barrier layer, $M_i^{\chi+}$ is interstitial cation, M_M is metal cation on the metal sublattice of the barrier layer, $V_{\ddot{O}}$ is oxygen vacancy on the oxygen sublattice of the barrier layer, O_O is oxygen anion on the oxygen sublattice of the barrier layer, $M^{\delta+}$ is metal cation in solution.

Inconel,[48] with an assumption that the barrier layer of the passive films upon such alloys is a point-defective single-phase Cr_2O_3. During transpassive dissolution of such alloys, the steady-state current density was found to increase exponentially with the increasing anodic potential, whereas the thickness of the barrier layer decreased linearly with the increasing anodic potential.[48] The PDM successfully accounts for such changes during transpassive dissolution of SPEAs exhibiting a single-oxide barrier layer. In contrast, the thickness of the multi-oxide barrier layer of the AlTiVCr alloy was found to increase during transpassive dissolution of V and Cr.[22] Therefore, the presence of multiple passive elements in significant fractions may result in a contrasting film growth behavior (unique to SPEAs) owing to the formation of the multi-oxide film. However, the role of multi-oxide structure on growth kinetics of the passive film upon alloys remains undiscussed, which might be due to the inability of conventional methodologies in ascertaining the complex and competing interfacial processes.

Recently, the AESEC approach has been very successful in revealing the element-resolved dissolution behavior of complex (multi-elemental) alloys.[49,50] AESEC is based on real-time analysis of the electrolyte using in-line inductively coupled plasma mass spectroscopy (ICP-MS) or optical emission spectroscopy (ICP-OES), during electrochemical testing.[51] The AESEC approach has been used to investigate key factors of the passivity upon a growing list of alloys (including MPEAs). Examples of new insights revealed by AESEC include selective dissolution,[50] transpassive dissolution,[52] enrichment, and repassivation.[22] In addition to primary dissolution-based analysis, AESEC has also been used to investigate the growth of the passive film upon pure metals;[53] however, the growth behaviour of the multi-oxide passive films upon MPEAs remains unstudied.

Herein the AESEC method was applied, together with XPS and Mott-Schottky analysis, to investigate the growth kinetics of the multi-oxide film upon AlTiVCr, during both potentiodynamic and potentiostatic polarisation in 0.6 M NaCl. Previous studies have revealed that AlTiVCr alloy exhibits excellent corrosion resistance ascribed to a multi-oxide passive film composed of Al_2O_3, TiO_2, V_2O_3, and Cr_2O_3.[22,54] Moreover, the alloy exhibits a wide passive window and excellent repassivation behaviour, despite transpassive dissolution of V and Cr during anodic polarisation. Therefore, the evolution of growth kinetics of the film during transpassive dissolution of V and Cr was studied herein and was discussed in the context of the PDM.

Experimental

Material.—The equiatomic AlTiVCr alloy (comprised of 25 at.% of each element) was cast via arc melting on a water-cooled copper mold in an argon atmosphere. The starting materials were high purity metals (>99.95%), and the ingot was remelted several times to ensure chemical homogeneity. The as-solidified specimen was successively ground to a 4000 grit SiC paper finish, followed by cloth polishing with a 1 μm colloidal silica suspension. Detailed microstructural analysis of the alloy may be found in a previous paper.[55,56] The AlTiVCr alloy exhibits a single-phase microstructure with an ordered BCC (B2) structure.

Atomic emission spectroelectrochemistry.—The AESEC testing was carried out in 0.6 M NaCl using a radial electrochemical flow cell (ALS Co. Ltd., Japan) and using an SP-50 Biologic potentiostat. The electrochemical flow cell consisted of a sample working electrode, an Ag/AgCl (3 M NaCl) reference electrode (+209 mV vs SHE), and a stainless-steel tube as the counted electrode. In-line inductively coupled plasma mass spectroscopy (ICP-MS, NexION 2000 PerkinElmer) was used to determine the real-time composition of the electrolyte during electrochemical measurements. Prior to electrochemical testing, standard electrolyte samples were analysed to determine the correlation factor between concentration and intensity, to convert the obtained elemental intensity into elemental concentration. The flow rate of the electrolyte through the cell was 240 μl min^{-1}. Open circuit potential (OCP) was stabilised for initial 1800 s, followed by potentiodynamic polarisation from −200 mV vs OCP to 1.8 V_{SHE} at a scan rate of 1 mV s^{-1}.

In a prior study,[22] the passive film upon the AlTiVCr alloy was found to be a multi-oxide film enriched with Al_2O_3 and TiO_2 at OCP, in 0.6 M NaCl. During anodic polarisation, however, transpassive dissolution of V and Cr leads to the formation of secondary and tertiary passive windows, respectively. A staircase potentiostatic polarisation test was performed to further investigate the dissolution and growth kinetics of the passive film during transpassive dissolution of V and Cr. After 1800 s of OCP (~−0.1 V_{SHE}) measurement, the specimen was potentiostatically polarised at 0.7 V_{SHE}, followed by 1.1 V_{SHE}, each for 900 s.

The dissolution current density for each alloying element was calculated using Eq. 4.

$$j_m = \delta F\left(\frac{fC_m}{M_m A}\right), \quad [4]$$

where F is the Faraday constant (96485 C), M_m is the molar mass of the dissolving element m (in g mol^{-1}), f is the flow rate of the electrolyte (in cm^3 s^{-1}), C_m is the concentration of dissolved element m in the downstream electrolyte (in g cm^{-3}) and A is the exposed surface area (in cm^2). The term $\frac{fC_m}{M_m A}$ represents the dissolution rate of element m (in mol cm^{-2} s^{-1}). The charge (δ) of Al, Ti, V, and Cr cations in the electrolyte at OCP were +3, +4, +3, and +3, respectively. However, the charge of V and Cr cations were changed to +5 and +6, respectively, for calculation of respective elemental current densities during their transpassive dissolution. The charge stored in the form of surface film during potentiodynamic and potentiostatic polarization can be calculated by subtracting the total dissolution current ($j_{diss} = j_{Al} + j_{Ti} + j_V + j_{Cr}$) from external anodic current (j_{ext}) and integrating with real time.[50]

$$q_{film} = \int_0^t (j^* - j_{diss})dt \quad [5]$$

Here j^*_{ext} is the convolution integral of j_{ext}, which can be expressed as:

$$j^* = \int_0^t j_{ext}(\tau)h(t-\tau)d\tau \quad [6]$$

Here h(t) is the residence time distribution (RTD), which can be expressed as a log-normal function (Eq. 7).[51]

$$h(t) = \sqrt{\frac{\eta}{\pi\tau^2}}\, e^{\frac{-1}{4\eta}} e^{-\eta \ln^2\left(\frac{t}{\tau}\right)} \quad [7]$$

Here the values of η and τ were empirically determined to be 0.99 and 40 s, respectively, using the approach proposed by Ogle et al. (for pure Cu in HCl solution).[49]

The obtained charge density of the film was further converted into the film thickness using Eq. 8.

$$L = \left(\frac{M_{film}}{\chi F \rho_{film}}\right) q_{film} \quad [8]$$

where M_{film} and ρ_{film} are the molecular mass and the density of the film, and χ is the cationic charge in the oxide.

X-ray photoelectron spectroscopy.—The composition and thickness evolution of the passive film formed at different anodic potentials were determined using X-ray photoelectron spectrometer. The primary, secondary, and tertiary passive films were developed following 1 h hold at the OCP, +0.7 V_{SHE}, and +1.1 V_{SHE}, respectively. Thereafter, XPS analysis was performed using a Thermo NEXSA XPS system, which was equipped with Al Kα X-ray source (1486.7 eV) and a

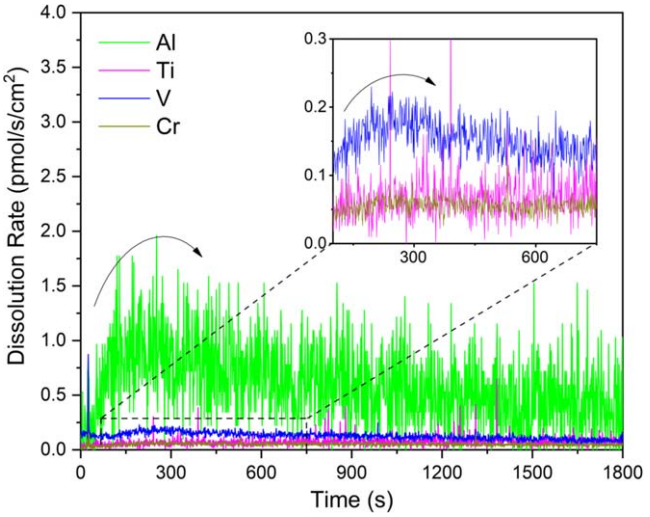

Figure 2. AESEC dissolution profile of AlTiVCr at OCP in quiescent 0.6 M NaCl (at 25 °C).

multichannel resistive plate detector. High-resolution XPS spectra for Al 2p, Ti 2p, V 2p, Cr 2p, and O 1s photoelectrons were collected at a step size of 0.1 eV and at a take-off angle of 90º. Deconvolution and quantification analysis was performed using *Avantage* software.

Mott-Schottky analysis.—The passive films upon most metals and alloys are reported to be semiconductors.[7] Therefore, the electronic properties of the film including the nature and density of point defects (including vacancies and interstitials) control the growth kinetics of the film. The evolution of the electronic properties of the film during transpassive dissolution and the subsequent effect on growth kinetics of the film were studied using Mott-Schottky analysis. The Mott-Schottky analysis was performed in a flat bottom electrochemical cell consisting standard calomel reference electrode (+244 mV vs SHE), a platinum mesh as counter electrode, and the specimen as working electrode. Initially, the specimens were cathodically polarised at −0.8 V_{SHE} for 300 s to remove the air-born films. Just after the cathodic cleaning, three different specimens were held at open circuit potential, +0.7 V_{SHE} and +1.1 V_{SHE} for 1 h to grow the primary, secondary, and tertiary passive film respectively. The capacitance of film-electrolyte interface ($C_{f/s}$) was measured in the potential range from +1.2 V_{SHE} to −0.3 V_{SHE} with a potential sweep rate of 50 mV s^{-1}. In this regard, electrochemical impedance spectroscopy (EIS) was performed at a single frequency (f) of 1 kHz and a sine wave of 10 mV amplitude. Similar parameters are used in the case of passive metals and alloys.[57–59] The apparent capacitance can be estimated from the imaginary part of the interfacial impedance (Z″) using Eq. 9.

$$C_{f/s} = \frac{1}{2\pi f Z''} \quad [9]$$

The equivalent circuit used herein contains a resistor and a capacitor in series, which is adequate provided that the frequency is on the order of kHz. The influence of surface states and current leakage can be excluded using such a high frequency.

The interfacial capacitance can be further expressed by Eq. 10, with an assumption that both the space charge capacitance (C_{SC}) and Helmholtz double-layer capacitance (C_H) are in series.

$$\frac{1}{C_{f/s}} = \frac{1}{C_{SC}} + \frac{1}{C_H} \quad [10]$$

Here C_H can be assumed to be constant (~20 μF cm^{-2}).[57,60,61] However, the change in C_{SC} with respect to applied potential (E) can be expressed by the Mott-Schottky equation (Eq. 11):

$$\frac{1}{C_{SC}^2} = \frac{\pm 2}{\epsilon\epsilon_0 eN}\left(E - E_{fb} - \frac{kT}{e}\right) \quad [11]$$

Here ϵ is the dielectric constant of the film, ϵ_0 is the vacuum permittivity (8.85×10^{-14} F cm^{-1}), e is the elementary charge (1.6×10^{-19} C), N is the density of ionic defects (also known as donor or acceptor for n-type or p-type semiconductor, respectively). E_{fb} is the flatband potential (degree of bending of band-edge), k is Boltzmann constant and T represents the temperature. The value of $\frac{kT}{e}$ is approximately 25.6 mV for ambient temperature. A positive slope between $\frac{1}{C_{SC}^2}$ and E is obtained for n-type semiconductor, whereas p-type semiconductor exhibits a negative slope.

Results

Element-resolved dissolution analysis.— *Open circuit potential.*—The dissolution profile of the AlTiVCr alloy at the OCP is shown in Fig. 2.

It is noted from Fig. 2 that the dissolution rate of Al was comparatively higher than that of the other three elements at the OCP. It may be readily observed that the dissolution rate of Al started increasing as soon as the specimen was exposed to the electrolyte, and followed a decreasing trend after 250 s of open circuit immersion. The dissolution rate of V which was much lower than that of Al, followed a similar trend. On the other hand, dissolution rates of Ti and Cr remained negligible and steady during open circuit immersion, suggesting immediate incorporation into the passive film.

Potentiodynamic polarisation.—Figure 3a shows the AESEC potentiodynamic polarisation curve of the AlTiVCr alloy following 1800 s at the OCP in 0.6 M NaCl. The dissolution current densities of all four elements were calculated using Eq. 4.

It is seen that the total dissolution current density (j_{diss}) at the OCP (−0.1 V_{SHE}) was ~10^{-7} A cm^{-2}, indicating excellent corrosion resistance of the AlTiVCr alloy in 0.6 M NaCl. Moreover, the total dissolution current density remained steady until +0.1 V_{SHE} during anodic polarisation. The dissolution current of V started increasing exponentially with the increase in anodic potential above +0.1 V_{SHE} and reached a steady value above +0.4 V_{SHE}. The total dissolution current density that was mainly contributed by the dissolution current density of V at this stage, followed a similar trend with the increasing anodic potential. Such behavior was posited to the transpassive dissolution of V, which was also confirmed by the predicted E-pH diagram in a previous work.[22] The dissolution current density of Cr increased exponentially with the increase in anodic potential above +0.8 V_{SHE}, suggesting transpassive dissolution of Cr. With further increase in anodic potential, the dissolution current density attained another steady region above +1.0 V_{SHE}.

It is seen that the dissolution rate of Al also increased to some extent during transpassive dissolution of V and Cr. Such secondary effect is believed to be due to acidification of adjacent electrolytes, associated with the transpassive dissolution reaction. The dissolution rate of Ti remained steady and negligible during transpassive dissolution of V and Cr, suggesting significant enrichment of Ti on the alloy surface during anodic polarisation. The final breakdown at +1.4 V_{SHE}, resulted in a significant increase in dissolution rates of all four elements, which was hypothesised to be due to the combined effect of oxygen evolution reaction (OER) and transpassive dissolution. However, the dissolution rate of Ti was relatively small compared with that of the other three elements, suggesting continual enrichment of Ti on the AlTiVCr surface during the final breakdown.

During anodic polarisation, the total dissolution current density (j_{diss}) was lower than the external current density (j_{ext}), suggesting

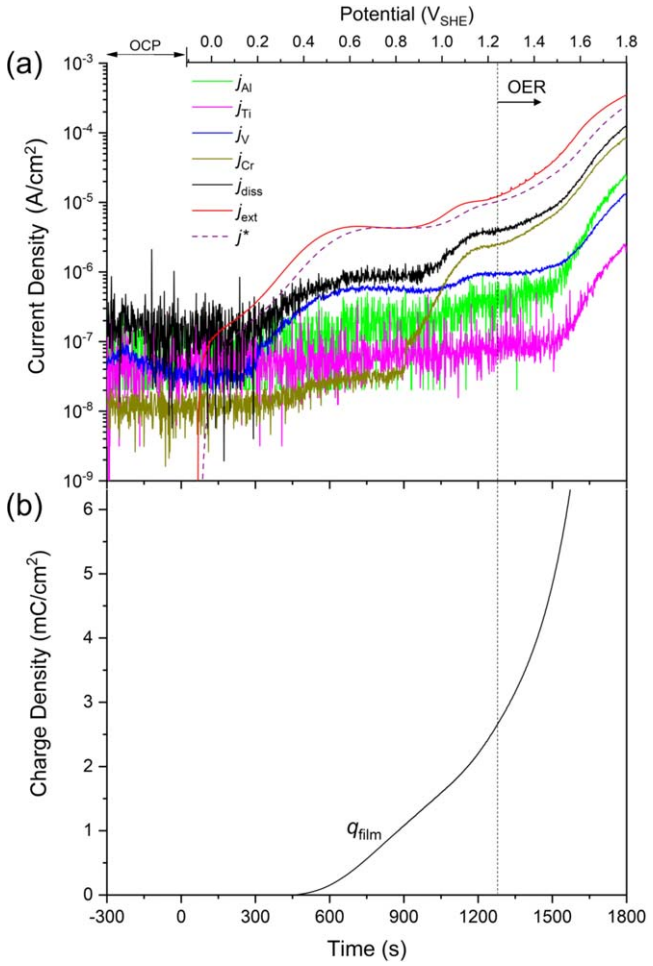

Figure 3. AESEC dissolution profile of AlTiVCr during anodic potentiodynamic polarisation in 0.6 M NaCl (at 25 °C): (a) Dissolution current densities of all four elements, (b) Charge density of the film.

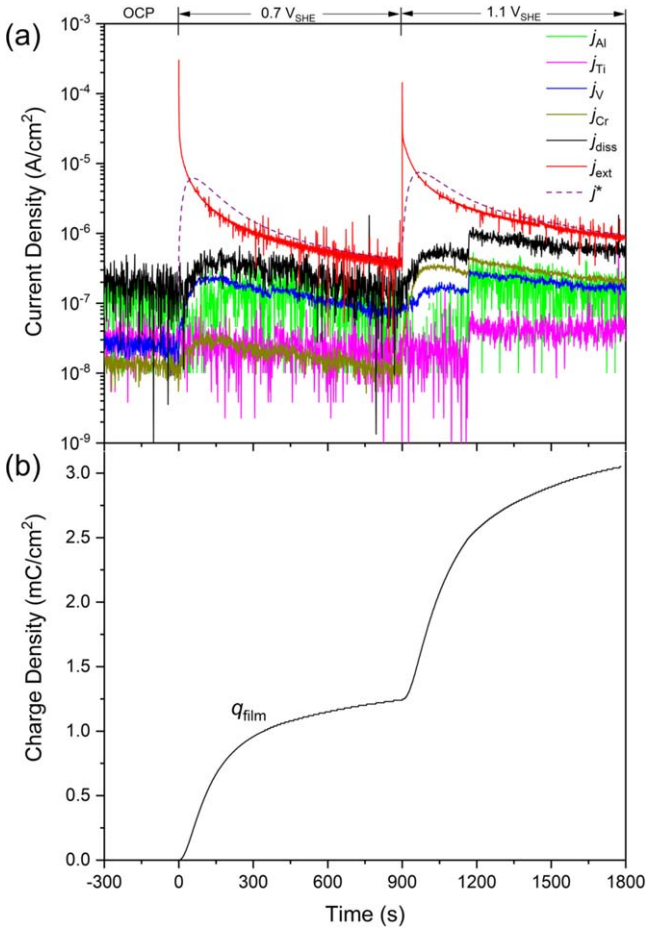

Figure 4. AESEC dissolution profile of AlTiVCr during anodic staircase-potentiostatic polarisation in 0.6 M NaCl (at 25 °C): (a) Dissolution current densities of all four elements, (b) Charge density of the film.

significant charge incorporation into the surface film (Fig. 3a). Charge balance analysis was carried out in order to quantify the formation of the film. The charge density of the film (q_{film}) obtained using Eq. 5 is shown in Fig. 3b. It is seen from Fig. 3b that the charge density of film increased linearly with the increase in applied potential, with changing slope at different passive windows. The value of $j_{ext} - j_{diss}$ increased exponentially above +1.2 V_{SHE} due to the OER. Therefore, the charge balance analysis for the film calculation is not applicable in the OER region. The value of dq_{film}/dE increased with transpassive dissolution of V, and further during transpassive dissolution of Cr. It suggests that the growth rate of the passive film has increased during transpassive dissolution of the alloy.

Potentiostatic polarisation.—After 1800 s of OCP stabilisation, a potential step to +0.7 V_{SHE} (i.e., in the secondary passive region) resulted in a sharp increase in the dissolution current of V, owing to the transpassive dissolution (Fig. 4a). The dissolution current of V showed the maximum at around 150 s (of potentiostatic polarisation at +0.7 V_{SHE}), thereafter followed a gradual decrease with further increase in the polarisation time. During potentiostatic polarisation at +0.7 V_{SHE}, the dissolution currents of Al and Cr also increased to some extent and started decreasing along with V, whereas the dissolution current of Ti remained unaltered. The total dissolution current density initially increased until 150 s of potentiostatic polarisation and started decreasing with increasing polarisation time. Moreover, the total dissolution current density decreased to the value of the primary passive window (i.e., 10^{-7} A cm^{-2}) in 900 s of potentiostatic polarisation. With increasing polarisation time, the difference between the external current density and dissolution current density decreased, suggesting a decrease in the growth rate of the film with increasing film thickness.

The second potential step was applied, from +0.7 V_{SHE} (secondary passive region) to +1.1 V_{SHE} (tertiary passive region) to study the effect of transpassive dissolution of Cr. It is seen from Fig. 4a that the dissolution current of Cr increased significantly at this stage. Similar to the first potential step, the dissolution current of Cr reached a maximum after 1050 s (i.e., 150 s at +1.1 V_{SHE}) and started decreasing with increasing polarisation time. At this stage, the dissolution currents of Al and V also increased, whilst Ti yet again remained unaffected. Total dissolution current density decreased until 1200 s (i.e., 300 s at +1.1 V_{SHE}), where dissolution currents of all four elements increased abruptly and immediately started decreasing with increasing the polarisation time. This sudden increase of the dissolution currents, however, did not affect the external current, suggesting a localised breakdown followed by quick repassivation of the film. The total dissolution current density decreased with further increase in polarisation time and reached a steady value of 5×10^{-7} A cm^{-2} in 1800 s.

For potentiostatic polarisation, the charge density of the film (q_{film}) was found to increase logarithmically with time (Fig. 4b). It can also be seen that the charge density of the film formed at +1.1 V_{SHE} is significantly higher than that at +0.7 V_{SHE}. This behavior is consistent with the potentiodynamic behavior, suggesting that the thickness of the film has further increased during transpassive dissolution of Cr.

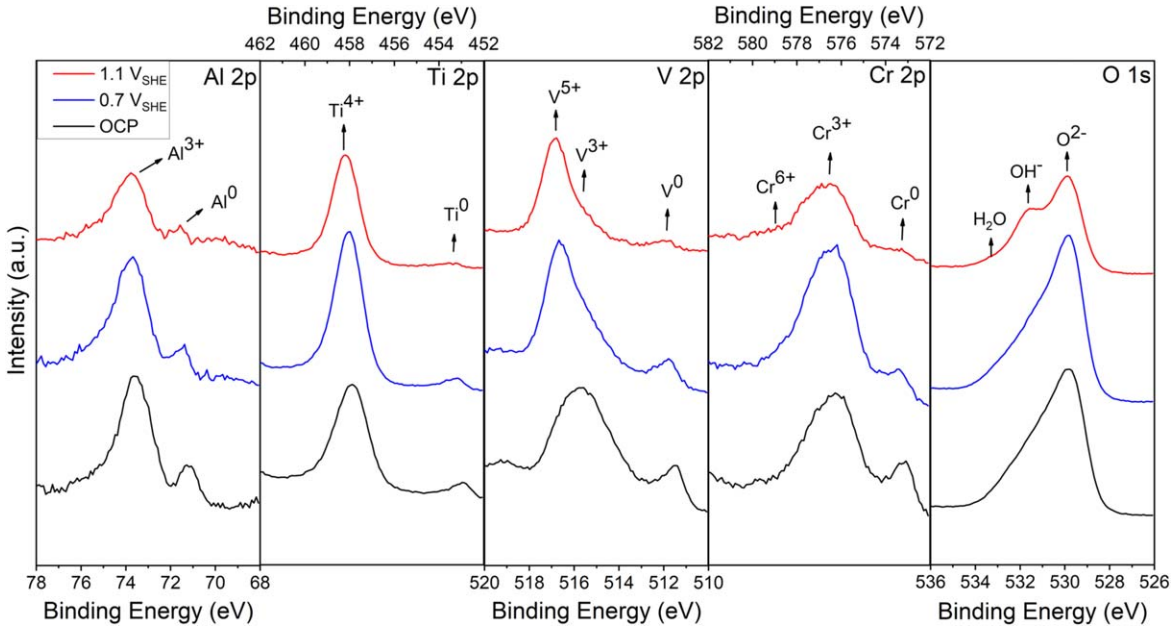

Figure 5. XPS spectra of all elements present in the surface film formed upon AlTiVCr from exposure in 0.6 M NaCl (at 25 °C) at the OCP, +0.7 V_{SHE}, and +1.1 V_{SHE}.

X-ray photoelectron spectroscopy analysis.—High-resolution XPS spectra of Al 2p, Ti 2p, V 2p, Cr 2p, and O 1s core for the surface films formed at OCP (primary film), +0.7 V_{SHE} (secondary film), and +1.1 V_{SHE} (tertiary film) are shown in Fig. 5.

The $2p_{3/2}$ peaks obtained at 74.6 eV, 458.5 eV, 515.3 eV, and 557.7 eV confirm the presence of Al_2O_3, TiO_2, V_2O_3, and Cr_2O_3, respectively in the film.[62–64] V was also present in a pentavalent (V^{5+}, at 517.3 eV)[63] state in all three films, which may be in the form of hydroxides. The presence of V^{5+} species confirms the transpassive dissolution of V_2O_3 by transforming into water-soluble V^{5+} oxide. Similarly, the presence of a small fraction of hexavalent chromium (Cr^{6+}, at 579.5 eV)[64] in the tertiary film confirms the transpassive dissolution of Cr_2O_3 above +0.8 V_{SHE}.

A detailed quantification analysis can be found in a previous paper.[22] Obtained cationic fractions in the films are given in Table I. It may be readily observed that all three films are enriched with Al_2O_3 and TiO_2. However, the volume fraction of TiO_2 increased and the volume fraction of Al_2O_3 decreased significantly with the increase in anodic potential. Moreover, the overall volume fractions of oxides/hydroxides of V and Cr remained unchanged during transpassive dissolution of V and Cr.

An approach based on inelastic mean free paths (IMFPs) of photoelectrons was taken to estimate the thickness of the films. The detailed calculation methods and the parameters are given in the Appendix. The thickness of the primary, secondary, and tertiary passive films were estimated to be 4.2 nm, 6.2 nm, 7.7 nm, respectively (Table I), using the approach proposed by Strohmeier.[65] Moreover, the thickness of the barrier layers of the primary, secondary and tertiary films were estimated to be 2.1 nm, 3.8 nm, and 5.3 nm, respectively (Table I), using the approach proposed by Olsson and Landolt.[66] It was noted that the change in thickness of the outer precipitation layer was negligible with the increase in anodic potential (Table I). Therefore, the XPS results suggest that the thickness of the barrier layer increases with the increase in anodic potential despite transpassive dissolution of V and Cr. Moreover, the increase in the barrier layer thickness during transpassive dissolution of V and Cr was mainly contributed by the growth of TiO_2 in the film.

Semiconductor properties of the film.—The Mott-Schottky (MS) analysis following 1 h of potentiostatic polarisation, was carried out in order to investigate the electronic properties of the primary, secondary and tertiary passive films. The obtained potentiostatic polarisation curves and Mott-Schottky plots are shown in Figs. 6 and 7, respectively.

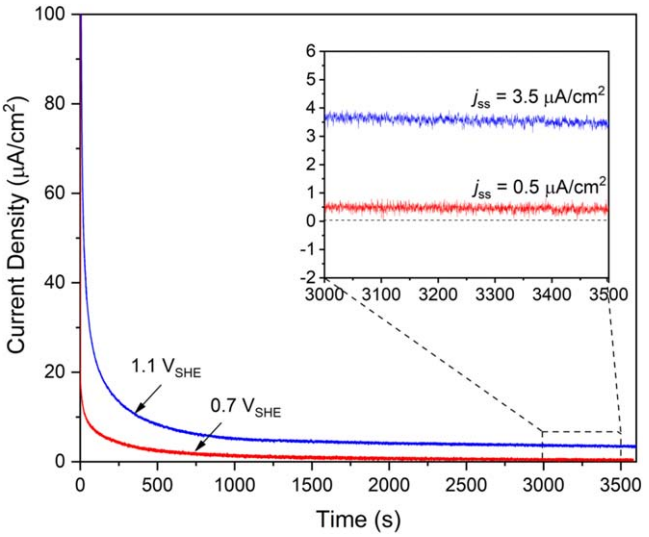

Figure 6. Potentiostatic polarisation curves of AlTiVCr, obtained at +0.7 V_{SHE} and +1.1 V_{SHE} in quiescent 0.6 M NaCl (at 25 °C).

The Mott-Schottky plot exhibiting a positive slope indicates n-type semiconductor behavior of the passive film (Fig. 7a). Al_2O_3 and TiO_2, which also happened to be predominating oxides in the film, are known to display n-type semiconductor behavior.[67,68] Therefore, the obtained n-type behavior of the passive film can be credited to the enrichment of Al_2O_3 and TiO_2. However, low voltage p-type behavior could be due to the presence of Cr_2O_3.[69] This complex behavior in the Mott-Schottky plot with a knee point is also found in Cr-containing SPEAs, which is mainly believed to represent p-n junction in the passive film.[69,70]

The n-type film may contain two types of donors (or positive charge carriers): metal interstitials and oxygen vacancies. Metal interstitials are dominating at low potential, whereas oxygen vacancies dominate at higher applied potential.[69] The donor density

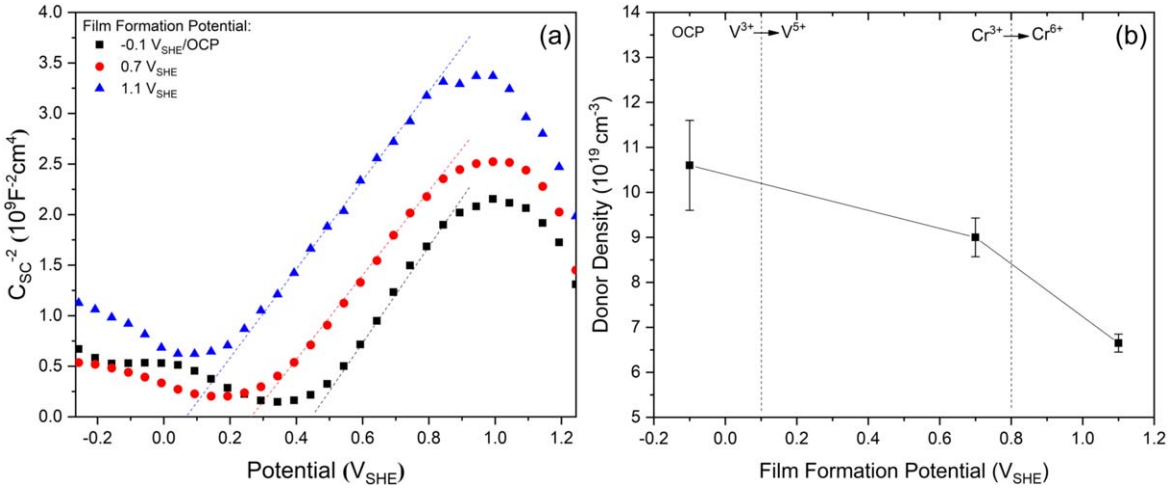

Figure 7. Properties of surface films formed upon AlTiVCr following 1 h of exposure in 0.6 M NaCl (at 25 °C) at OCP, +0.7 V_{SHE}, and +1.1 V_{SHE}: (a) Mott-Schottky plot, and (b) Donor density.

can be estimated from Eq. 11, if the dielectric constant of the film is known. It is however challenging to determine the dielectric constant for a multi-oxide film. For simplicity, we consider the barrier layers of all three films as binary composites, as the films are mainly composed of Al_2O_3 and TiO_2. With such assumption, the dielectric constant of the barrier film can be estimated using the effective medium theory (EMT) formula (Eq. 12) that is used for predicting the dielectric constant of binary composites.[71]

$$\epsilon_{mix} = \epsilon_M \left[1 + \frac{v_D(\epsilon_D - \epsilon_M)}{\epsilon_M + sv_M(\epsilon_D - \epsilon_M)} \right] \quad [12]$$

Here s (=0.165) is a constant, ϵ_M and ϵ_D are the dielectric constants of the matrix and dispersion phase, respectively. v_M and v_D are the volume fraction of the matrix and dispersion phase, respectively. There are many empirical equations proposed for binary composites, with the EMT formula being most suitable for the case high ϵ_D/ϵ_M.[71] The values of dielectric constants of the films formed at the OCP (primary film), +0.7 V_{SHE} (secondary film), and +1.1 V_{SHE} (tertiary film) were estimated to be 37, 42, and 48, respectively, with the assumption that Al_2O_3 ($\epsilon_M = 9$)[67] is the matrix and TiO_2 ($\epsilon_D = 56$)[68] is the dispersion phase of the films. The calculated donor densities of the films are plotted with respect to film formation potential in Fig. 7b. It may be readily seen from Fig. 7b that the donor density of the passive film decreased with increasing anodic potential despite transpassive dissolution of V, and further with transpassive dissolution of Cr. It indicates that transpassive dissolution has increased the annihilation rate of oxygen vacancy, suggesting an increase in the growth rate of film during transpassive dissolution.

The flatband potentials of the films formed at the OCP, +0.7 V_{SHE} and +1.1 V_{SHE} were estimated to be +0.425 V_{SHE}, +0.250 V_{SHE}, and +0.050 V_{SHE}, respectively, using Eq. 10. It suggests that the flatband potential shifted towards less noble potential with transpassive dissolution of V and further with transpassive dissolution of Cr. In general, the flatband potential is independent of the film formation potential; however, it may change with the compositional evolution of the film as well as of the electrolyte.[72] Transpassive dissolution leads to a change in the film composition as well as a decrease in the interfacial pH. The flatband potentials of most (semiconductor) oxides reported to shift toward noble potential with the decrease in pH.[73] Therefore, a negative shift of the flatband potential during transpassive dissolution of V and Cr can be credited to the change in the film composition.

Discussion

The predicted E-pH suggests that all four oxides of the passive film, i.e. Al_2O_3, TiO_2, V_2O_3, and Cr_2O_3, are thermodynamically stable at the OCP.[22] Based on XPS results (Fig. 5 and Table I), it is assumed that the barrier layer of the passive film on the AlTiVCr alloy is comprised of a complex (composite type) mixture of Al_2O_3, TiO_2, V_2O_3, and Cr_2O_3. Al_2O_3 can be considered as the parent oxide matrix, whereas TiO_2, V_2O_3, and Cr_2O_3 are the dispersion oxides. Esmaily et al. characterised the oxide scale of the AlTiVCr alloy formed at high temperatures (i.e., 700 °C and 900 °C) using electron microscopy and X-ray diffraction, and confirmed the presence of such multi-oxide structure.[74] In that work, it was also found that Al_2O_3 and TiO_2 were distributed throughout the layer, whereas Cr_2O_3 and V_2O_3(+V_2O_5) were present in the innermost layer and outermost layer, respectively. Al_2O_3 is comparatively less resilient to chloride attack despite a wide stability potential window in neutral electrolytes. Therefore, the presence of protective TiO_2, V_2O_3, and Cr_2O_3 in the Al_2O_3 matrix is the key factor for the excellent corrosion resistance of the primary passive film. Moreover, the dissolution profile at the OCP (Fig. 2) suggests that an optimal enrichment of such protective oxides is essential to make the multi-oxide film "passive".

The AESEC dissolution analysis revealed that V and Cr undergo transpassive dissolution above +0.1 V_{SHE} and +0.8 V_{SHE} respectively, during anodic polarisation in 0.6 M NaCl (Figs. 3 and 4). Transpassive dissolution of interstitial oxides, V_2O_3 and Cr_2O_3 can be presented by Reactions 8 and 9, respectively, which suggest that the interfacial pH decreases during such oxidative dissolution.

$$V_2O_3 + 5H_2O \rightarrow 2VO_4^{3-}(aq) + 10H^+ + 4e^- \quad [R8]$$

$$Cr_2O_3 + 5H_2O \rightarrow 2CrO_4^{2-}(aq) + 10H^+ + 6e^- \quad [R9]$$

The Al_2O_3 rich barrier layer matrix dissolves by Reaction 10.

$$Al_2O_3 + 6H^+ \rightarrow 2Al^{3+} + 3H_2O \quad [R10]$$

The dissolution rate of the Al_2O_3 is independent of applied potential as there is no change in oxidation state ($\chi = \delta$, in Eq. 2). However, the decrease in the interfacial pH can increase the dissolution rate of the Al_2O_3 rich barrier layer (Eq. 2 and Reaction 10). Therefore, the increase in the dissolution rate of Al during transpassive dissolution can be attributed to the decrease in the interfacial pH. However, the dissolution rate of Ti was very small relative to that of the other three elements during both transpassive dissolution events. The XPS results (Table I) suggest that Ti, being enriched on the alloy surface, spontaneously formed stable TiO_2 and resulted in a thickening of the multi-oxide film. It indicates that the growth of stable TiO_2 is predominately, if not entirely, responsible for the increase in thickness of the barrier layer of the multi-oxide film during transpassive dissolution of V and Cr.

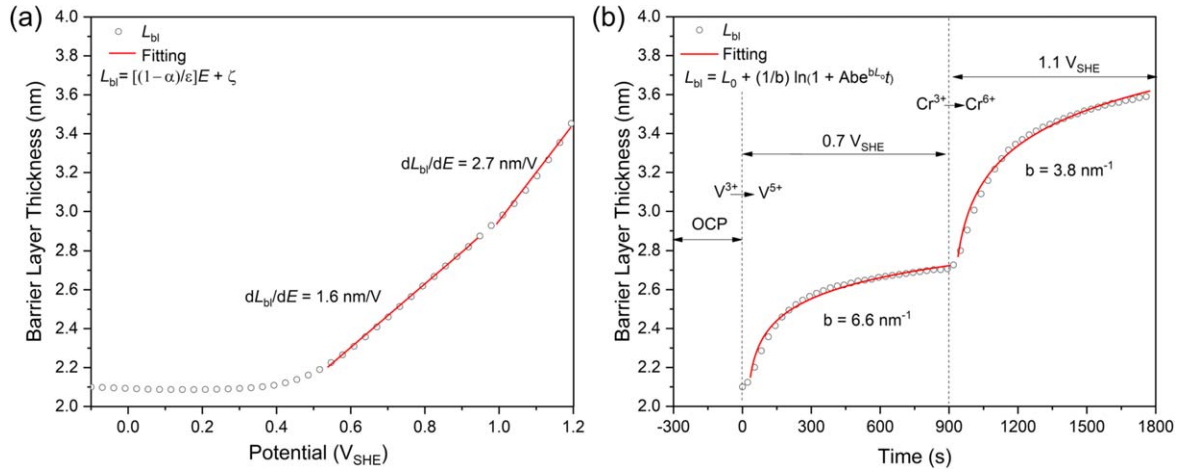

Figure 8. Change in thickness of barrier oxide layer of multi-oxide passive film upon AlTiVCr during anodic potentiodynamic polarisation and staircase potentiostatic polarisation in 0.6 M NaCl (at 25 °C).

Therefore, it can be assumed that charge accumulation on the surface during anodic polarisation was mainly associated with the growth of TiO_2 in the film. The thickness of the outer layer remained unchanged during anodic polarisation (Table I); therefore, the change in the film thickness during anodic polarisation was mainly associated with the barrier layer. The term $\frac{M_{film}}{\chi F \rho_{film}}$ in Eq. 8 was estimated to be 4.89×10^{-5} cm^3 C^{-1} for TiO_2 (cationic charge = +4, molar mass = 79.86 g mol^{-1}, and density = 4.23 g cm^{-3}). With such assumption, the charge density of the film obtained using the AESEC charge-balance analysis was converted into the thickness of the film using Eq. 8. The obtained growth behavior of the barrier layer during potentiodynamic polarisation and staircase potentiostatic polarisation is shown in Fig. 8. The thickness of the barrier layer of film formed at the OCP (L_0) was 2.1 nm, as estimated using XPS (Table I).

As seen in Reaction 10, there is no change in oxidation state of Al cation during the dissolution of the Al_2O_3 rich barrier layer matrix. Thus, Eq. 3 becomes:

$$L_{ss} = \frac{1}{\varepsilon}[1 - \alpha]E + \zeta \qquad [13]$$

Here $\zeta = \frac{1}{\varepsilon}\left\{\frac{2.303n}{\alpha_3\chi\gamma} - \beta\right\}pH + \frac{1}{\alpha_3\chi K}\ln\left(\frac{k_3^0}{k_7^0}\right)$, which is independent of the applied potential. Although the dissolution rate of Al increased during transpassive dissolution of V and Cr, the average dissolution rate was estimated to be 5×10^{-6} nm s^{-1}. Therefore, the value of C is sufficiently small that the term "Ct" can be neglected and $e^{-bCt} = 1 + bCt$, in Eq. 2. Consequently, Eq. 2 yields the classical logarithmic relationship (Eq. 14).

$$L(t) = L_0 + \frac{1}{b}[1 + Abe^{-bL_0}t] \qquad [14]$$

The solid red lines in Figs. 8a and 8b are the best fits to Eqs. 13 and 14, respectively. As seen from Fig. 8, the thickness of the barrier layer of the film increases: (a) linearly with the increase in anodic potential, and (b) logarithmically with the increase in the time of potentiostatic polarisation. As listed in Table II, similar growth kinetics has been reported in the case of most metals and SPEAs.[23–25,27–31,37,75,76] It may be readily observed that the value of $\frac{dL}{dE}\left(=\frac{1}{\varepsilon}[1 - \alpha]\right)$ increased and the value of b decreased with increasing anodic potential, suggesting the value of electric field (ε) has decreased with transpassive dissolution of V and Cr. By assuming $\alpha = 0.5$, the values of the electric field strength for the barrier layer formed at +0.7 V_{SHE} and +1.1 V_{SHE} were estimated to be 0.3×10^6 V cm^{-1} and 0.18×10^6 V cm^{-1}, respectively. TiO_2 exhibits lower resistivity than Al_2O_3 at ambient temperature;[77] the potential drop through the barrier layer is expected to decrease with the increasing fraction of TiO_2. Therefore, the decrease in the electric field through the barrier layer can be attributed to the composition evolution of the film (i.e. enrichment of TiO_2) owing to transpassive dissolution of V and Cr. The decrease in the electric field through the film due to transpassive dissolution has also been reported in the case of stainless steel,[31] which was also hypothesized to be due to the change in the film composition.

Direct-logarithmic growth behavior (Fig. 8b) indicates that the limiting factor for the growth of the multi-oxide film on the AlTiVCr alloy is transport of ionic species through the film. The Mott-Schottky analysis (Fig. 7b) revealed that the film is an n-type semiconductor, growth of which is mainly controlled by transport of oxygen vacancies. In general, the density of oxygen vacancy decreases exponentially with the increase in anodic potential within a passive window.[78] However, the density of oxygen vacancy was reported to re-increase during transpassive dissolution of pure metals and conventional alloys.[79,80] It is mainly hypothesised that the density of cation vacancy (of dissolving element) increases at the film-electrolyte interface during transpassive dissolution, which subsequently leads to acceleration in generation of oxygen (cation) vacancy at the metal-film interface in order to accomplish charge neutrality within the film.[80] On the contrary, the density of oxygen vacancy in the multi-oxide film upon the AlTiVCr alloy was found

Table I. Composition and thickness of the film formed upon AlTiVCr in 0.6 M NaCl (at 25 °C) at OCP, +0.7 V_{SHE}, and +1.1 V_{SHE}.

	Cationic fraction in the film (at %)				Thickness (nm)	
Film formation potential	Al (Al_2O_3)	Ti (TiO_2)	V (V_2O_3 + V^{5+})	Cr (Cr_2O_3 + Cr^{6+})	Barrier layer	Precipitation layer
OCP	46	24	15	15	2.1	2.1
0.7 V_{SHE}	43	26	15	16	3.8	2.4
1.1 V_{SHE}	41	30	16	13	5.3	2.4

Table II. Reported growth kinetics of the passive films upon pure metals and conventional alloys.

Metal /Alloy	Electrolyte	Technique	Growth kinetics of the film		References
			With applied potential	With exposure duration	
Fe	Borate buffer, Phosphate buffer (pH = 1.85 − 11.50)	Coulometric, Ellipsometry	Linear	Direct-logarithmic	Sato et al.[37]
	Borate buffer (pH = 8.4)	Coulometric, Ellipsometry	Linear	Inverse-logarithmic	Goswami et al.[27]
Ni	1 N H_2SO_4	Coulometric	Linear	Inverse-logarithmic	Zamin et al.[75]
Cu	0.1 M $Na_2B_4O_7$ + 1 M $LiClO_4$	Potential pulse	Linear	Direct-logarithmic	Lohrengel et al.[76]
Ti	EG + 0.6 M H_2O + (0.004, 0.015, 0.027) mol-dm^{-3} NH_4F	Impedance, XPS, Photocurrent	Linear	Direct-logarithmic	Bojinov et al.[23]
Al, Ta, Nb, Zr, Hf, Mo	0.1 M: Na_2SO_4, NaCl, $NaNO_3$, Na_3PO_4, NaBr, KI, $(COO)_2Na_2$, CH_3COONa	Impedance	Linear	Direct-logarithmic	Gad-Allah et al.[24]
Zr, Nb, W	0.4 M Na_2SO_4 + 0.1 H_2SO_4	Micro-balance	Linear	Direct-logarithmic	Olsson et al.[25]
316 SS	5 N H_2SO_4	Coulometric, Ellipsometry	Linear	Direct-logarithmic	Bulman et al.[28]
	0.5 M NaCl	Impedance	Linear	Inverse-logarithmic	Ferreira et al.[29]
Fe, 430 SS	Borate buffer (pH = 8.4)	X-ray reflectivity	Linear	Direct-logarithmic	Kim et al.[31]
Fe-25Ni-xCr (x = 0, 5, 10, 16, 30)	Borate buffer (pH = 8.7)	Ellipsometry	Linear	Direct-logarithmic	Silverman et al.[30]
Fe-10Ni, Fe-10Cr, Fe-10Ni-10Cr	Borate buffer (pH = 8.4)	Coulometric, Ellipsometry	Linear	Inverse-logarithmic	Goswami et al.[27]
AlTiVCr-MPEA	0.6 M NaCl	AESEC, XPS	Linear[a)]	Direct-logarithmic	Current study

a) Potentiodynamic polarization.

to decrease with increasing anodic potential, despite transpassive dissolution (Fig. 7b). One possible explanation for such behavior could be the increase in the diffusivity of oxygen vacancies in the film. Sikora et al. proposed that the diffusivity of oxygen vacancies through the film (D_O) is directly proportional to flux of oxygen vacancy at the alloy-film interface (j_O), and inversely proportional to the electric field (Eq. 15).[78]

$$D_O = \frac{j_O RT}{2F\omega\epsilon}, \qquad [15]$$

where ω is a constant. The flux of oxygen vacancy $j_O \left(=\frac{j_{ss}}{2e}\right)$ can be obtained from the steady-state current density (j_{ss}). As seen in Fig. 6, the steady-state current density, and therefore, the generation rate (or flux) of oxygen vacancy at the alloy-film interface increased with transpassive dissolution. Moreover, the value of the electric field was found to be decreasing with transpassive dissolution. Therefore, the diffusivity of oxygen vacancies also increased during transpassive dissolution of the multi-oxide film upon the AlTiVCr alloy. Higher diffusivity of oxygen vacancies through the film would lead to a higher rate of annihilation at the film-electrolyte interface, which can be credited to the higher growth rate of the barrier layer of the film during transpassive dissolution of V and Cr. According to the PDM, the electric field through the single-oxide barrier layer and the diffusivity of oxygen vacancies are independent of anodic potential. For the multi-oxide film, however, both the electric field and diffusivity of oxygen vacancies may change with the composition evolution of the film.

In summary, transpassive dissolution of V and Cr led to an increase in the dissolution rate of Al_2O_3 and enrichment of TiO_2 in the barrier layer of the multi-oxide film. Consequently, the electric field within the barrier layer decreased and the growth rate of the barrier layer increased during both transpassive dissolution. As proposed by the PDM, an increase in thickness of the barrier layer leads to a decrease in potential drop at the alloy-film interface that increases the potential barrier for further oxidation of the alloy.[81] Consistent with the PDM, the growth rate of the multi-oxide film upon the AlTiVCr alloy decreases exponentially with the increase in exposure duration during potentiostatic polarisation. Thus, the work herein suggests that the PDM can also provide an accurate account of the growth behavior of the multi-oxide passive films on MPEAs. The electric field across such film however, changes with the evolution of film composition owing to incongruent formation and dissolution behavior of constitutional oxides.

Conclusions

The growth and protection mechanism of the passive film upon the multi principal element alloy AlTiVCr, under anodic polarisation, was presented. AlTiVCr was found to exhibit a multi-oxide passive film with the barrier layer enriched Al_2O_3 and TiO_2, resulting in excellent corrosion resistance and a wide passive window, despite transpassive dissolution of V and Cr in 0.6 M NaCl.

The dissolution rate of Al was found to increase during transpassive dissolution of V and Cr, which was attributed to the decrease in pH of the adjacent electrolyte. The thickness of the passive film was found to increase with continual enrichment of TiO_2 during anodic polarisation. Moreover, the passive film upon the alloy was found to obey direct-logarithmic growth kinetics, similar to the most passive metals and conventional single-principal element alloys. Consistent with the point defect model (PDM), the thickness of the barrier layer of the film increased linearly with increasing anodic potential (during potentiodynamic polarisation) and logarithmically with increasing exposure duration (during potentiostatic polarisation). The electric field across the barrier layer was found to be dependent on the film composition, and decreased with an increasing fraction of TiO_2, owing to a decrease in resistivity of the barrier layer. It was observed using the Mott-Schottky analysis that the density of oxygen vacancy decreased with increasing anodic potential despite transpassive dissolution. This was attributed to an increase in the diffusivity of oxygen vacancies during transpassive dissolution of V and Cr, resulting in an increased oxygen vacancy annihilation rate, and hence, an increased growth rate of TiO_2 in the barrier layer. The present work emphasises that the growth and protection mechanism of complex passive films upon multi-principal element alloys using the PDM, taking the evolution of the film composition into account.

Acknowledgments

The authors gratefully acknowledge the use of facilities in Monash Analytical Platform and Monash X-ray Platform (MXP). The authors would like to thank Dr. Yao Qiu for the technical assistance. SC is supported by an MGS scholarship.

Appendix : Estimation of Thickness of Passive Film Using XPS

The approximate thickness of the passive film (predominantly containing Al_2O_3) formed upon Al -alloys can be determined using Eq. A·1:[65]

$$L = \lambda_{Al}^{ox} \sin\theta \ln\left(1 + \frac{I_{Al}^{ox} c_{Al}^{met} \lambda_{Al}^{met}}{I_{Al}^{met} c_{Al}^{ox} \lambda_{Al}^{ox}}\right) \qquad [A·1]$$

where, λ_{Al}^{ox} and λ_{Al}^{met} are IMFPs of Al 2p photoelectron in the film and the metal phase, respectively. I_{Al}^{ox} and I_{Al}^{met} represent the XPS peak intensities of Al in the film and the metal phase, respectively. c_{Al}^{ox} and c_{Al}^{met} are the atomic fractions of Al in the film and the metal phase, respectively. θ represents the take-off angle of photoelectrons. I_{Al}^{ox}, I_{Al}^{met}, c_{Al}^{ox}, and c_{Al}^{met} were obtained from quantification analysis using *Avantage* software. Moreover, IMFPs (λ_{Al}^{ox} and λ_{Al}^{met}) of Al 2p photoelectrons were estimated using the TPP-2 formula (Eq. A·2), proposed by Tanuma et al.[82]

$$\lambda = \frac{E}{{E_p}^2\left[p \ln\left(\frac{0.191E}{\sqrt{\rho}}\right) - \left(\frac{G}{E}\right) + \left(\frac{H}{E^2}\right)\right]} \qquad [A·2]$$

where

$$p = -0.0216 + 7.4 \times 10^{-4}\rho + \frac{0.944}{\sqrt{{E_p}^2 + {E_g}^2}} \qquad [A·3]$$

$$G = 1.97 - 0.91\left(\frac{\rho N_v}{M}\right) \qquad [A·4]$$

$$H = 53.4 - 20.8\left(\frac{\rho N_v}{M}\right) \qquad [A·5]$$

Here, E is the electron energy in eV, $E_p \left(=28.8\sqrt{\frac{\rho N_v}{M}}\right)$ is the free electron plasmon energy, ρ is the density, N_v is the number of valence electrons per atom (for elements) or molecule (for oxides), M is the molecular mass, and E_g is the energy bandgap (in eV). Using Eq. A·2, λ_{Al}^{ox} and λ_{Al}^{met} were obtained to be 3.14 nm and 3.10 nm, respectively. Moreover, thicknesses of the films formed at the OCP, 0.7 V_{SHE}, and 1.1 V_{SHE} were calculated to be 4.2 nm, 6.2 nm, and 7.8 nm, respectively. Furthermore, the thickness of the outer layer (L_{ol}) can be estimated using Eq. A·6, proposed by Olsson and Landolt.[66]

$$L_{ol} = -\lambda_O^{ox} \sin\theta \ln\left(\frac{1 + g_1 e^{-\frac{L}{\lambda_O^{ox}\sin\theta}}}{1 + g_1 + g_1 g_2\left(1 - e^{-\frac{L}{\lambda_O^{ox}\sin\theta}}\right)}\right) \qquad [A·6]$$

where

$$g_1 = \frac{I_{OH}^{ox} c_O^{ox}}{I_O^{ox} c_{OH}^{ox}} \quad [A\cdot7]$$

$$g_2 = \frac{I_{H_2O}^{ox} c_{OH}^{ox}}{I_{OH}^{ox} c_{H_2O}^{ox}} \quad [A\cdot8]$$

Here λ_O^{ox} is the IMFP of O 1s photoelectron in the film. I_O^{ox}, I_{OH}^{ox} and $I_{H_2O}^{ox}$ are the peak intensities of O^{2-}, OH^- and water peak, respectively. c_O^{ox}, c_{OH}^{ox} and $c_{H_2O}^{ox}$ represent the concentrations of O^{2-}, OH^- and water in the film, respectively. The value of λ_O^{ox} was obtained to be 2.331 nm, using Eq. A·2. The thickness of the barrier layer (L_{bl}) of the film can be estimated using Eq. A·9.

$$L_{bl} = L - L_{ol} \quad [A\cdot9]$$

ORCID

S. Choudhary https://orcid.org/0000-0003-0296-9811

References

1. O. N. Senkov, J. D. Miller, D. B. Miracle, and C. Woodward, *Calphad Comput. Coupling Phase Diagrams Thermochem.*, **50**, 32 (2015).
2. N. Birbilis, S. Choudhary, J. R. Scully, and M. L. Taheri, *npj Mater. Degrad.*, **5**, 14 (2021).
3. D. B. Miracle and O. N. Senkov, *Acta Mater.*, **122**, 448 (2017).
4. Y. Zhang, T. T. Zuo, Z. Tang, M. C. Gao, K. A. Dahmen, P. K. Liaw, and Z. P. Lu, *Prog. Mater Sci.*, **61**, 1 (2014).
5. Y. Shi, B. Yang, and P. K. Liaw, *Metals*, **7**, 43 (2017).
6. J. R. Scully, S. B. Inman, A. Y. Gerard, C. D. Taylor, W. Windl, D. K. Schreiber, P. Lu, J. E. Saal, and G. S. Frankel, *Scr. Mater.*, **188**, 96 (2020).
7. J. W. Schultze and M. M. Lohrengel, *Electrochim. Acta*, **45**, 2499 (2000).
8. S. Choudhary, S. O. Brien, Y. Qiu, S. Thomas, R. K. Gupta, and N. Birbilis, *Electrochem. Commun.*, **125**, 106989 (2021).
9. Y. Shi, B. Yang, X. Xie, J. Brechtl, K. A. Dahmen, and P. K. Liaw, *Corros. Sci.*, **119**, 33 (2017).
10. H. Luo, Z. Li, A. M. Mingers, and D. Raabe, *Corros. Sci.*, **134**, 131 (2018).
11. C. Dai, H. Luo, J. Li, C. Du, Z. Liu, and J. Yao, *Appl. Surf. Sci.*, **499**, 143903 (2020).
12. L. Wang, D. Mercier, S. Zanna, A. Seyeux, M. Laurent-Brocq, L. Perrière, I. Guillot, and P. Marcus, *Corros. Sci.*, **167**, 108507 (2020).
13. X. W. Qiu, *J. Alloys Compd.*, **555**, 246 (2013).
14. Y. Qiu, R. Liu, T. Gengenbach, O. Gharbi, S. Choudhary, S. Thomas, H. L. Fraser, and N. Birbilis, *npj Mater. Degrad.*, **4**, 1 (2020).
15. X. L. Shang, Z. J. Wang, Q. F. Wu, J. C. Wang, J. J. Li, and J. K. Yu, *Acta Metall. Sin. (English Lett.)*, **32**, 41 (2019).
16. H. Torbati-Sarraf, M. Shabani, P. D. Jablonski, G. J. Pataky, and A. Poursaee, *Mater. Des.*, **184**, 108170 (2019).
17. Q. T. Song and J. Xu, *Corros. Sci.*, **167**, 108513 (2020).
18. Y. J. Hsu, W. C. Chiang, and J. K. Wu, *Mater. Chem. Phys.*, **92**, 112 (2005).
19. Y. Qiu, S. Thomas, D. Fabijanic, A. J. Barlow, H. L. Fraser, and N. Birbilis, *Mater. Des.*, **170**, 107698 (2019).
20. J. Jayaraj, C. Thinaharan, S. Ningshen, C. Mallika, and U. Kamachi Mudali, *Intermetallics*, **89**, 123 (2017).
21. M. Pourbaix, *Atlas of Electrochemical Equilibria in Aqueous Solutions* (NACE, Houston) (1974).
22. S. Choudhary, Y. Qiu, S. Thomas, and N. Birbilis, *Electrochim. Acta*, **362**, 137104 (2020).
23. M. Bojinov, I. Betova, and V. Karastoyanov, *Electrochim. Acta*, **344**, 136137 (2020).
24. A. G. Gad-Allah, H. A. Abd El-Rahman, and M. M. Abou-Romia, *Br. Corros. J.*, **23**, 181 (1988).
25. C.-O. A. Olsson, M.-G. Vergé, and D. Landolt, *J. Electrochem. Soc.*, **151**, B652 (2004).
26. N. Sato, T. Noda, and K. Kudo, *Electrochim. Acta*, **19**, 471 (1974).
27. K. N. Goswami and R. W. Staehle, *Electrochim. Acta*, **16**, 1895 (1971).
28. G. M. Bulman and A. C. C. Tseung, *Corros. Sci.*, **13**, 531 (1973).
29. M. G. S. Ferreira, *J. Electrochem. Soc.*, **132**, 760 (1985).
30. S. Silverman, G. Cragnolino, and D. Macdonald, *J. Electrochem. Soc.*, **129**, 2419 (1982).
31. D. H. Kim, S. S. Kim, H. H. Lee, H. W. Jang, J. W. Kim, M. Tang, K. S. Liang, S. K. Sinha, and D. Y. Noh, *J. Phys. Chem. B*, **108**, 20213 (2004).
32. C. Lukac, J. B. Lumsden, S. Smialowska, and R. W. Staehle, *J. Electrochem. Soc.*, **122**, 1571 (1975).
33. Z. Szklarska-Smialowska and W. Kozlowski, *J. Electrochem. Soc.*, **131**, 234 (1984).
34. W. Kozlowski and J. Flis, *Corros. Sci.*, **28**, 787 (1988).
35. J. Kruger and J. P. Calvert, *J. Electrochem. Soc.*, **114**, 43 (1967).
36. F. P. Fehlner and N. F. Mott, *Oxid. Met.*, **2**, 59 (1970).
37. N. Sato and M. Cohen, *J. Electrochem. Soc.*, **111**, 512 (1964).
38. C. Y. Chao, L. F. Lin, and D. D. Macdonald, *J. Electrochem. Soc.*, **128**, 1187 (1981).
39. N. Cabrera and N. F. Mott, *Reports Prog. Phys.*, **12**, 163 (1949).
40. F. Brown and W. D. Mackintosh, *J. Electrochem. Soc.*, **120**, 1096 (1973).
41. M. A. H. Lanyon and B. M. W. Trapnell, *Proc. R. Soc. Lond. A. Math. Phys. Sci.*, **227**, 387 (1955).
42. D. D. Macdonald, *Electrochim. Acta*, **56**, 1761 (2011).
43. D. D. Macdonald, M. Al Rifaie, and G. R. Engelhardt, *J. Electrochem. Soc.*, **148**, B343 (2001).
44. G. R. Engelhardt, B. Kursten, and D. D. Macdonald, *Electrochim. Acta*, **313**, 367 (2019).
45. F. Mao, J. Yao, Y. Zhou, C. Dong, B. Kursten, and D. D. Macdonald, *Corros. Sci.*, **154**, 239 (2019).
46. D. D. Macdonald and G. R. Engelhardt, *ECS Trans.*, **28**, 123 (2010).
47. Y. Zhang, D. D. Macdonald, M. Urquidi-Macdonald, G. R. Engelhardt, and R. B. Dooley, *Corros. Sci.*, **48**, 3812 (2006).
48. D. D. Macdonald, A. Sun, N. Priyantha, and P. Jayaweera, *J. Electroanal. Chem.*, **572**, 421 (2004).
49. K. Ogle and S. Weber, *J. Electrochem. Soc.*, **147**, 1770 (2000).
50. K. Ogle, J. Baeyens, J. Swiatowska, and P. Volovitch, *Electrochim. Acta*, **54**, 5163 (2009).
51. K. Ogle, *Corrosion*, **75**, 1398 (2019).
52. J. D. Henderson, X. Li, D. W. Shoesmith, J. J. Noël, and K. Ogle, *Corros. Sci.*, **147**, 32 (2019).
53. L. Jiang, P. Volovitch, U. Sundermeier, M. Wolpers, and K. Ogle, *Electrochim. Acta*, **58**, 322 (2011).
54. Y. Qiu, S. Thomas, R. K. Gupta, T. Gengenbach, R. Jones, and N. Birbilis, *Corrosion*, **74**, 1312 (2018).
55. Y. Qiu, Y. J. Hu, A. Taylor, M. J. Styles, R. K. W. Marceau, A. V. Ceguerra, M. A. Gibson, Z. K. Liu, H. L. Fraser, and N. Birbilis, *Acta Mater.*, **123**, 115 (2017).
56. Y. Qiu, S. Thomas, M. A. Gibson, H. L. Fraser, K. Pohl, and N. Birbilis, *Corros. Sci.*, **133**, 386 (2018).
57. P. Acevedo-Peña, J. Vazquez-Arenas, R. Cabrera-Sierra, L. Lartundo-Rojas, and I. González, *J. Electrochem. Soc.*, **160**, C277 (2013).
58. M. A. Rodríguez and R. M. Carranza, *J. Electrochem. Soc.*, **158**, C221 (2011).
59. Y. Sun, A. Lan, M. Zhang, H. Yang, and J. Qiao, *Mater. Chem. Phys.*, **265**, 124509 (2021).
60. O. Gharbi, M. T. T. Tran, B. Tribollet, M. Turmine, and V. Vivier, *Electrochim. Acta*, **343**, 136109 (2020).
61. P. Schmuki, H. Böhni, and J. A. Bardwell, *J. Electrochem. Soc.*, **142**, 1705 (1995).
62. J. Zähr, S. Oswald, M. Türpe, H. J. Ullrich, and U. Füssel, *Vacuum*, **86**, 1216 (2012).
63. M. C. Biesinger, L. W. M. Lau, A. R. Gerson, and R. S. C. Smart, *Appl. Surf. Sci.*, **257**, 887 (2010).
64. M. C. Biesinger, B. P. Payne, A. P. Grosvenor, L. W. M. Lau, A. R. Gerson, and R. S. C. Smart, *Appl. Surf. Sci.*, **257**, 2717 (2011).
65. B. R. Strohmeier, *Surf. Interface Anal.*, **15**, 51 (1990).
66. C. O. A. Olsson and D. Landolt, *Corros. Sci.*, **46**, 213 (2004).
67. F. J. Martin, G. T. Cheek, W. E. O'Grady, and P. M. Natishan, *Corros. Sci.*, **47**, 3187 (2005).
68. A. M. Schmidt, D. S. Azambuja, and E. M. A. Martini, *Corros. Sci.*, **48**, 2901 (2006).
69. J. Yao, D. D. Macdonald, and C. Dong, *Corros. Sci.*, **146**, 221 (2019).
70. N. B. Hakiki, S. Boudin, B. Rondot, and M. Da Cunha Belo, *Corros. Sci.*, **37**, 1809 (1995).
71. W. S. Chen and M. Y. Hsieh, *Ceram. Int.*, **43**, S343 (2017).
72. J. M. Bolts and M. S. Wrighton, *J. Phys. Chem.*, **80**, 2641 (1976).
73. Y. Yu, K. A. Click, S. C. Chien, J. Sun, A. Curtze, L. C. Lin, and Y. Wu, *J. Phys. Chem. C*, **123**, 8681 (2019).
74. M. Esmaily, Y. Qiu, S. Bigdeli, M. B. Venkataraman, A. Allanore, and N. Birbilis, *npj Mater. Degrad.*, **4**, 25 (2020).
75. M. Zamin, *J. Electrochem. Soc.*, **126**, 470 (1979).
76. M. Lohrengel, J. Schultze, H. Speckmann, and H.-H. Strehblow, *Electrochim. Acta*, **32**, 733 (1987).
77. H. Unno, Y. Sato, S. Toh, N. Yoshinaga, and S. Matsumura, *J. Electron Microsc. (Tokyo).*, **59**, 107 (2010).
78. E. Sikora, J. Sikora, and D. D. Macdonald, *Electrochim. Acta*, **41**, 783 (1996).
79. E. Sikora and D. D. Macdonald, *Electrochim. Acta*, **48**, 69 (2002).
80. C. Man, C. Dong, Z. Cui, K. Xiao, Q. Yu, and X. Li, *Appl. Surf. Sci.*, **427**, 763 (2018).
81. D. D. Macdonald, *J. Electrochem. Soc.*, **137**, 2395 (1990).
82. S. Tanuma, C. J. Powell, and D. R. Penn, *Surf. Interface Anal.*, **20**, 77 (1993).